Tailorable Stimulated Brillouin Scattering in a Partially Suspended Aluminium Nitride Waveguide in the Visible Range

Peng Li,[1] Jize Yan,[1,*] Jun-Yu Ou[2] and Goran Z. Mashanovich[2]

[1] School of Electronics and Computer Science, University of Southampton,Southampton SO17 1BJ, United Kingdom
[2] Optoelectronics Research Centre, University of Southampton,Southampton SO17 1BJ, United Kingdom
[*] J.Yan@soton.ac.uk

Abstract: Stimulated Brillouin scattering (SBS) has been widely applied in narrow line-width laser, microwave filters, optical gyroscopes and other fields. However, most research is limited within near-infrared to mid-infrared range. This is due to the limited transparent window in most materials, such as silicon and germanium. Aluminium Nitride (AlN) is a novel III-V material with a wide transparent window from 200 nm and an appropriate refractive index to confine the light. In this paper, we first validate the full-vectorial formalism to calculate SBS gain based on the measured results from a silicon platform. Compared to previous researches, our model achieves higher accuracy in terms of frequency, Q factor as well as Brillouin gain coefficient without modifying the waveguide width. It also reveals the importance of matching rotation matrix and crystalline coordinate system. Then, we investigate the SBS in a partially suspended AlN waveguide at 450 nm based on the validated method. It shows a wide tunability in frequency from 16 GHz to 32 GHz for forward SBS and a range from 42 GHz to 49 GHz for backward SBS. We numerically obtain the value of Brillouin gain of 1311 $W^{-1}m^{-1}$ when Q factor is dominated by anchor loss for forward SBS of TE mode. We also find out that in the case for forward SBS of TM mode, anchor loss could be greatly suppressed when the node point of the selected acoustic mode matches with the position of pillar anchor. Our findings pave a new way to obtain Brillouin-related applications in integrated photonic circuit within the visible range.

1. Introduction

Stimulated Brillouin scattering (SBS) is a third-order nonlinear effect originating from the coupling between optical and acoustic waves [1,2]. Although SBS has initially been considered as a detrimental effect in optical fibre systems, there are more and more applications of SBS in narrow line-width laser [3–5], microwave photonics filters [6–8], non-reciprocal component [9,10], light storage [11,12], and optical gyroscopes [13]. Recently it is predicted that in nanoscale waveguide the increased radiation pressure due to the strong confinement of optical mode can lead to new forms of SBS nonlinearity in short length [14].

Since then, many different materials have been investigated to generate high SBS gain in integrated photonic circuits, such as chalcogenide glass [15,16], silicon [17–19], silicon nitride [20,21], AlGaAs [22] and GeSbS [23]. But most researchers have focused on the near-infrared range (NIR, ie.1.31-1.55 μm) due to the limitation of materials' transparent windows. Some materials, such as germanium, are extended for the SBS application at mid-infrared (MIR, ie 3.8 μm and above) due to its strong two photon absorption (TPA) and free-carrier absorption (FCA) induced by TPA at shorter wavelength [24,25].

However, there is a growing interest in investigating SBS at shorter wavelength. AlGaN-sapphire platform has been proposed as a potential candidate for achieving SBS in the visible range [26]. However, the difficulty of growing high crystal quality AlGaN has hindered this proposal [27].

Aluminium nitride (AlN) is another promising material for the application of SBS in the visible range. AlN has several distinct advantages. First, AlN has the largest energy gap of 6.2 eV among all the III-Nitride compounds [28]. This wide energy gap gives a transparent window from 200 nm and enables AlN to be free of TPA and FCA induced by TPA from 400 nm.

In addition, AlN has an appropriate refractive index of around 2 to confine the light and fairly big photoelastic constants (1.2 larger than that in GaN and 1.1 larger than that in Si) [28], which will be beneficial to enhance the Brillouin gain.

Besides, as a traditional material used in micro electrical-mechanical systems (MEMS), the deposition and fabrication of AlN is mature, and the roughness induced by fabrication can be well controlled [29, 30]. This decreases the propagation loss as well as the intrinsic loss of the mechanical energy.

Moreover, unlike silicon nitride, AlN can be deposited with low residual stress, permitting high confinement waveguides in both transverse electric (TE) and transverse-magnetic (TM) modes [31].

In this paper we propose a partially suspended AlN waveguide operating at 450nm to achieve high SBS gain. First we validate the accuracy of the full-vectorial method to calculate the Brillouin gain by matching the simulation results with the measured results of a silicon platform [17]. Then, based on our validated model, we simulate the forward SBS process (FSBS) and backward SBS process (BSBS) for TE mode and TM mode, separately. Our results indicate a strong coupling between optical and acoustic waves in our proposed platform. And it can reach a total gain of 1311 $W^{-1}m^{-1}$ for TE FSBS when both anchor loss and material loss are considered. Moreover, the anchor loss could be greatly suppressed due to the match between acoustic mode node point and the pillar position for TM FSBS. Our proposed waveguide systems exhibit new possibilities to explore the application of SBS in visible wavelength range and have potential applications in narrow-width laser and high-performance signal processing within the visible range.

2. Principle

2.1. Theory of calculating SBS gain from photoelasticity and moving boundary

In this section, we will present the formalism for calculating the SBS gain via photoelastic effect and moving boundary as proposed in [32]. In a translationally invariant waveguide system along the propagation axis (y-axis in this paper), the optical pump and Stokes waves can be approximately described as modulated optical eigenmode, with electric field distributions:

$$\mathbf{E_p}(r,t) = a_p(y,t)\cdot\widetilde{\mathbf{e_p}}(x,z)\cdot e^{i(\mathbf{k_p}\cdot y-\omega_p\cdot t)} + c.c. \tag{1}$$

$$\mathbf{E_s}(r,t) = a_s(y,t)\cdot\widetilde{\mathbf{e_s}}(x,z)\cdot e^{i(\mathbf{k_s}\cdot y-\omega_s\cdot t)} + c.c. \tag{2}$$

where $a_i(y,t)$ (with i=p,s) is the slowly-varying envelope function of the pump and Stokes waves, respectively. And $\widetilde{\mathbf{e_i}}(x,z)$ represent the spatial mode distribution, which are the solutions of the Helmholtz equations with wave vector $\mathbf{k_i}$ and angular frequency ω_i.

Similarly, the acoustic mode can also be written as :

$$\mathbf{U} = b(y,t)\widetilde{\mathbf{u}}(x,z)e^{j(\mathbf{q}\cdot y-\Omega_B\cdot t)} + c.c. \tag{3}$$

Where $b(y,t)$, $\mathbf{q}$ and Ω_B are the slowly varying envelope function, the wave vector and the angular frequency of the acoustic wave. The function $\widetilde{\mathbf{u}}(x,z)$ is the spatial distribution of the acoustic wave displacement, which is the solution of the following eigenvalue problem:

$$\rho\Omega_B^2\widetilde{u}_i + \sum_{ijkl}(\nabla_T + iq\hat{\mathbf{y}})_j c_{ijkl}(\nabla_T + iq\hat{\mathbf{y}})_k\widetilde{u}_l = 0. \tag{4}$$

Where i,j,k,l=(x,y,z), ρ and c_{ijkl} are the material density and the elastic tensor, respectively.

There are two mechanisms of the coupling between optical and acoustic modes. One contribution is from the photoelastic interaction Q_{PE} and the other is from the moving boundary Q_{MB}:

$$Q_{PE} = \varepsilon_0 \varepsilon_{core}^2 \int dr^2 \sum_{ijkl} e_i^{(s)*} e_j^{(p)} p_{ijkl} \partial_k \widetilde{u}_l^*. \tag{5}$$

$$\begin{aligned} Q_{MB} = \quad & \int_C dr(\hat{\mathbf{n}} \cdot \widetilde{\mathbf{u}}^*)[\varepsilon_0(\varepsilon_{core} - \varepsilon_{clad})(\widetilde{\mathbf{e}}_s \times \hat{\mathbf{n}})^* \cdot (\widetilde{\mathbf{e}}_p \times \hat{\mathbf{n}}) \\ & -\varepsilon_0^{-1}(\varepsilon_{core}^{-1} - \varepsilon_{clad}^{-1})(\widetilde{\mathbf{d}}_s \cdot \hat{\mathbf{n}})^* \cdot (\widetilde{\mathbf{d}}_p \cdot \hat{\mathbf{n}})]. \end{aligned} \tag{6}$$

Where ε_i (i=0,core,clad) are the permittivity for vacuum, core material and cladding material, respectively, and $\widetilde{\mathbf{d}}_i$ is the induction field. Eq. (5) is integrated over the whole transversal plane of the waveguide, while Eq. (6) is a line integral to be carried out along the waveguide boundaries with normal vector $\hat{\mathbf{n}}$ pointing from the core material to the cladding material.

Finally the total Brillouin gain can be calculated by means of:

$$G_0 = Q_m \cdot \frac{2\omega_p \left|Q_{PE} + Q_{MB}\right|^2}{P_p P_s P_B}. \tag{7}$$

Where Q_m, P_p, P_s and P_B are the mechanical quality factor, the pump, Stokes and acoustic modal power.

An efficient coupling between the optical and acoustic modes will only occur when the simultaneous conservation of energy and momentum [14] is satisfied.

$$\Omega_B = \omega_{\mathbf{p}} - \omega_{\mathbf{s}}. \tag{8}$$

$$\mathbf{q} = \mathbf{k_p} - \mathbf{k_s}. \tag{9}$$

Based on the fact that $\Omega_B \ll \omega_p, \omega_s$ and $\omega_p \approx \omega_s$, q is almost zero for FSBS while $q \approx 2k_p$ for BSBS [33]. The selected acoustic mode distribution will also match with the optical mode distribution [34].

The right part of Eq. (7) can be divided into two parts. Q_m reflects the mechanical energy loss. There are various sources leading to the decrease in Q_m [35]. The two main losses involved here are material loss and anchor loss [14].

Material loss can be calculated via the viscosity tensor of the material [17]. However, this data is not available for AlN. One way to estimate the $Q_{material}$ is via the Q×f product. The corresponding limit on $Q_{material}$ is bounded by the imposed limit on the Q×f product, which may be calculated for a given material [36]. Various results show that for AlN Q×f product is around the order of 10^{13} to 10^{14} [37–39]. For this paper where the acoustic frequency is ~ 10 GHz, Q factor can be estimated to have the upper bound $\sim 10^3$. Hence, we assume $Q_{material}$ to be 1000. This value might be overestimated, but it gives us a starting point to research the potential of AlN for the application of SBS at shorter wavelength.

As for the anchor loss Q_{anchor}, this can be numerically simulated by applying a perfectly matched layer (PML) [40] around the substrate. In the following section, the Q_m is the summation of these two sources ($Q_m^{-1} = Q_{material}^{-1} + Q_{anchor}^{-1}$).

For the remaining part (G_0/Q_m), this is defined as normalized gain coefficient g_0 [41]. This parameter indicates the intrinsic strength of the coupling between optical mode and acoustic mode, and is decided by material properties and waveguide shape [21]. The author will analyse normalized gain g_0 and Q_m separately to eliminate the uncertainty of the $Q_{material}$ in the following section.

2.2. Description of the material properties and the partially suspended system

To be able to simulate the optical mode and acoustic mode, the optical and mechanical properties of AlN and silica are required. AlN has a hexagonal wurtzite crystal structure, as shown in Fig. 1(a) [42], while silica is an amorphous material. This causes them to have different independent components for elastic constant tensor (a fourth-rank tensor), as shown in Table 1(a) [43]. Table 1(b) summarizes the optical and mechanical properties of AlN and silica [44–47]. The photoelastic constants (also a fourth-rank tensor) are also summarized within the table [28, 47]. It can be seen that AlN has a higher refractive index than silica at 450 nm, so the optical mode can be well confined in AlN via internal reflection. Meanwhile the acoustic velocity of AlN is higher than that of silica, so the acoustic mode inside AlN waveguide will naturally leak into the silica substrate. The realization of efficient Brillouin interactions requires the simultaneous confinements of the optical and acoustic waves. By partially etching the silica into a pillar anchor, the acoustic leakage could be greatly reduced. Such a design has also been adopted by the research in silicon [17] and lithium niobate [48] waveguides.

An illustration of our partially suspended AlN waveguide system is shown in Fig. 1(b). A total thickness h of 150nm AlN layer is developed on the silica substrate. The silica substrate is then partially etched to form a pillar anchor to decrease the acoustic wave leakage. d is the etching depth of the silica and g is the width of the pillar. In the following sections, g is fixed at 15nm. The width of waveguide w will be varied in the following study. The light propagates along the y-axis and the c-axis of the AlN coincides with the z-axis of the waveguide. While the a-axis of the AlN will have random rotation angle from the x-axis of the waveguide [31].

The reason for it is due to the mismatch of the crystal structure. It is difficult to grow pure single hexagonal crystal AlN on the top of amorphous silica. Instead, it will form “a thin polycrystalline film, consisting of columnar micrograins with c-axis oriented out-of-plane and random in-plane orientations" [31].

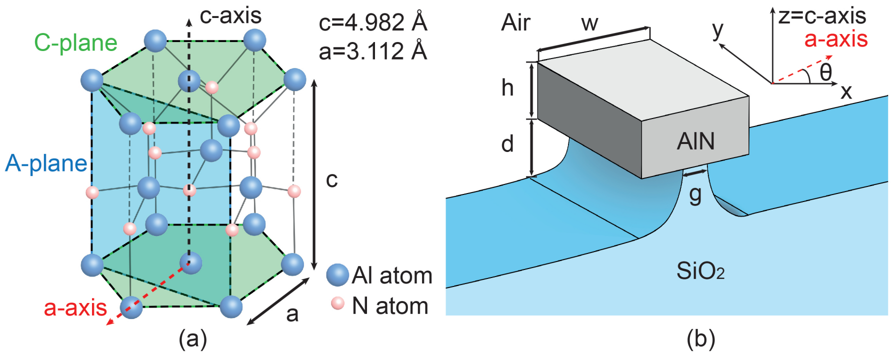

Fig. 1. (a) The hexagonal crystal structure of AlN [42]. (b) Schematic of the suspended systems; g=15nm, h=150nm, w is varied in the following section. The waveguide is aligned along the y-axis and the c-axis of the AlN coincides with the z-axis of the waveguide. Due to the mismatch of crystal structure, the a-axis of AlN has a random angle θ rotation from x-axis [31]. But such defect will not affect the whole performance of the system due to an unique characteristic called ‘transverse isotropy’ [49].

However, the hexagonal crystal structure of AlN has another unique characteristic called “transverse isotropy" [49]. For silicon and germanium with cubic crystal structure, different crystal orientation would alter the values of their fourth-rank tensors, thus leading to different SBS performance [24, 43]. But for hexagonal AlN, any rotation of the crystal structure around c-axis will not affect the value of any component in the fourth-rank tensor due to “transverse isotropy" [49] (More information see Supplementary 1). Thus, such a defect in the crystal orientation will not affect the whole performance of the system. This unique feature has relaxed the requirement for growing perfect single crystal AlN on amorphous silica.

Table 1. This table contains the structure of fourth-rank tensor for hexagonal AlN and amorphous silica (Voigt notation) [43]. The material parameters used for the investigation of Brillouin gain are also summarized in this Table: the refractive index n, density ρ and elastic tensor values c_{ij} are taken from [44–47]. The values for transverse and longitudinal velocities are calculated based on the density ρ and elastic tensor c_{ij}. The photoelastic tensor values are taken from [28, 47].

(a) Structure of fourth rank material tensors(Vogit notation)

AlN[0001](Wurtzite)	Silica(amorphous)
$\begin{pmatrix} a_{11} & a_{12} & a_{13} & 0 & 0 & 0 \\ a_{12} & a_{11} & a_{13} & 0 & 0 & 0 \\ a_{13} & a_{13} & a_{33} & 0 & 0 & 0 \\ 0 & 0 & 0 & a_{44} & 0 & 0 \\ 0 & 0 & 0 & 0 & a_{44} & 0 \\ 0 & 0 & 0 & 0 & 0 & a_{66} \end{pmatrix}$	$\begin{pmatrix} a_{11} & a_{12} & a_{12} & 0 & 0 & 0 \\ a_{12} & a_{11} & a_{12} & 0 & 0 & 0 \\ a_{12} & a_{12} & a_{11} & 0 & 0 & 0 \\ 0 & 0 & 0 & a_{44} & 0 & 0 \\ 0 & 0 & 0 & 0 & a_{44} & 0 \\ 0 & 0 & 0 & 0 & 0 & a_{44} \end{pmatrix}$

(b) Values of material parameters used for calculating Brillouin gain

quantity	unit	AlN[0001](Wurtzite)	Silica(amorphous)
n	–	2.15	1.45
ρ	kg/m^3	3230	2203
c_{11}	GPa	410	78.5
c_{12}	GPa	149	16.1
c_{13}	GPa	99	–
c_{33}	GPa	389	–
c_{44}	GPa	125	31.2
c_{66}	GPa	130.5	–
v_t	m/s	11270	5969
v_l	m/s	6220	3763
p_{11}	–	-0.1	0.121
p_{12}	–	-0.027	0.27
p_{13}	–	-0.019	–
p_{33}	–	-0.107	–
p_{44}	–	-0.032	-0.075
p_{66}	–	-0.037	–

3. Validation of the full-vectorial formalism for the calculation of Brillouin gain

To validate the accuracy of the equations and the model for calculating the Brillouin gain, the author first simulates a model based on a similar design in silicon platform [17]. Other researchers have also used [17] as a benchmark to test the accuracy of their models [50,51].

In [17], the waveguide is also partially suspended with a silica pillar support. The waveguide width is 450 nm and the height is 230 nm, the top of the pillar is 15 nm. And the waveguide is aligned along [110] axis of the silicon, all the fourth-rank tensor [elastic tensor $(c_{11}, c_{12}, c_{44}) = (166, 63.9, 79.6)$ GPa, photoelastic tensor $(p_{11}, p_{12}, p_{44}) = (-0.094, 0.017, -0.051)$, and viscosity tensor $(\eta_{11}, \eta_{12}, \eta_{44}) = (5.90, 5.16, 0.62)$ mPa·s] are rotated by $\pi/4$ from [100].

One aspect that can be easily overlooked here is that one has to match the rotation matrix with the crystal coordinate system. The failure to do so will lead to erroneous values in the elements of elastic tensor, photoelastic tensor, and viscosity tensor [24,43]. And the errors will be reflected in acoustic frequency (decided by elastic tensor), Brillouin gain coefficient (decided by photoelastic tensor), and most importantly Q_m (affected by viscosity tensor). Here, the author carefully sets the crystal coordinate system to match with the rotation matrix along z-axis. (More information see Supplementary 1). The results are summarized in Table 2.

Table 2. Summary of measured results from [17], author's simulated results when rotation matrix matches with crystal coordinate system and when they are unmatched, as well as the simulated results from [50,51]. In the author's model, the waveguide width is 450 nm as reported, and Q factor is calculated based on the material loss decided by viscosity tensor and anchor loss simulated via PML. In [50,51], the waveguide width is adjusted to 485 nm and the measured Q factor of 306 is directly applied. The author's results under matched condition achieve higher accuracy in terms of frequency, Q factor as well as normalized gain coefficient g_0, validating the accuracy of the author's model. It is also noticed that although g_0 under unmatched condition is similar to the matched condition, the frequency and the Q factor under unmatched condition is far away from the reported results.

Resource	Ω_{ac} (GHz)	Q factor	Normalized g_0 $(W^{-1}m^{-1})$
Measured results from [17]	9.2	306	10.52
Simulated results (matched condition)	9.285	339	10.18
Simulated results (unmatched condition)	9.92	585	10.14
Simulated results from [50]	9.2	306	9.5
Simulated results from [51]	9.212	306	9.53

It can be seen that the simulated results under matched condition are in good agreement with reported results in frequency, Q factor as well as the normalized gain coefficient g_0. Especially for g_0, the author's result only has 3% deviation compared to 9% of the reported results from previous model [50,51]. This validates the accuracy of the author's model.

It is also noticed that although the simulated results under unmatched condition are in good agreement with reported results in the normalized gain coefficient g_0, the frequency and Q factor are far away from the measured results.

Especially for Q factor, Fig. 2 shows the Q factor versus the ratio between pillar and waveguide width. It can be seen that the results under matched condition (blue line) can fit well with measured results (black dots) from [17], while the results under unmatched condition (red line) show big deviation from the measure results. This reveals the importance of the match between rotation matrix and crystal coordinate system.

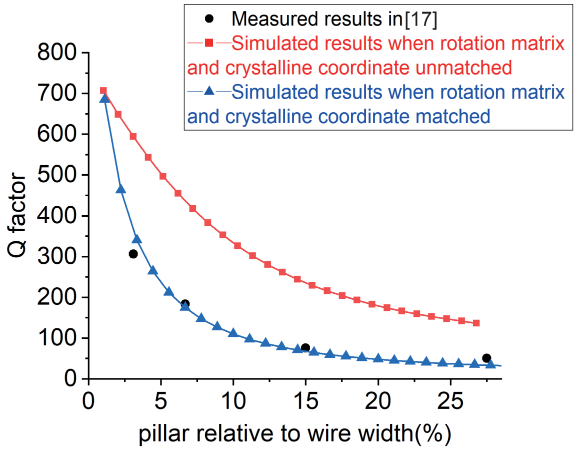

Fig. 2. Q factor versus the ratio between pillar and waveguide width: Measured results from [17] (black dot); Simulated results when rotation matrix and crystal coordinate unmatched (red line); Simulated results when rotation matrix and crystal coordinate matched (blue line). It can be seen that the results under matched condition can fit well with measured results from [17], showing the importance of the match between rotation matrix and crystal coordinate system.

Besides, the author did another simulation to investigate the potential reason for the difference between author's results and results from [50, 51]. A potential explanation is due to the different choice of rotation matrix and crystal coordinate system used in our method. Detailed analysis are not presented here for the sake of simplicity but it can be found in Supplementary 1 section 2.

In summary, the author validates the accuracy of the model and equations for calculating the Brillouin gain: our simulated results matches well with measured results from [17] in terms of the acoustic frequency, Q factor as well as the normalized gain coefficient g_0. It is realized without modifying the waveguide width and fixing the Q factor as what previous researchers do [50, 51]. In the following section, the author will investigate the SBS in our proposed partially suspended AlN waveguide based on this validated model.

4. Forward and backward stimulated Brillouin scattering for TE mode

First, the FSBS process for the TE mode is investigated. Fig. 3(a) shows the normalized electric field for TE mode, and the direction of E_x is parallel to the waveguide surface. According to the matching requirements of optical and acoustic mode distributions, the selected acoustic mode will also have a mode distribution with vibration along the x direction [34], as shown in Fig. 3(b).

Then waveguide width w is scanned from 160 nm to 320 nm. The change of refractive index n_0 and acoustic frequency ν_{TE}^{FSBS} versus the waveguide width w is plotted in Fig. 3(c). With w increasing, n_0 is getting bigger, indicating a better confinement of the optical mode. For acoustic frequency, the acoustic mode can be interpreted as the fundamental mode of a Fabry-Pérot cavity formed by the AlN/air boundary [17]. Its frequency can therefore be estimated as $\nu_{TE}^{FSBS} \approx V_t/2w$, where $V_t = \sqrt{C_{11}/\rho}$ is the transverse acoustic velocity. From Fig. 3(c) it can be seen that ν_{TE}^{FSBS} decreases reciprocally to the increasing w as predicted.

Fig. 3(d) summarizes the normalized gain coefficient g_0 (black), moving boundary contribution G_{MB} (blue), photoelastic contribution G_{PE} (red) and the Q_m (green). On one hand, with the increase of w, G_{MB} first slightly increases and then dramatically decreases to near zero. While G_{PE} will first increase and then gradually decreases to a stable level. This is because, with the waveguide getting wider, the optical mode is better confined within the AlN waveguide. This leads to more optical energy restrained within the waveguide and weaker intensity at the boundary, thus smaller G_{MB}. As for G_{PE}, it will initially benefit from the better confinement of the optical mode. But as w continues to increase, it will suffer from the decrease in optical intensity, and if the waveguide becomes wide enough, it will converge into the bulk condition.

On the other hand, Q_m increases almost linearly as w increases. A simplified explanation is via the relation between acoustic wavelength and anchor width g. With fixed g, as w increases, the acoustic frequency gets smaller, thus the wavelength gets larger. This increased wavelength will make it more difficult for the phonon to leak into the substrate via the anchor.

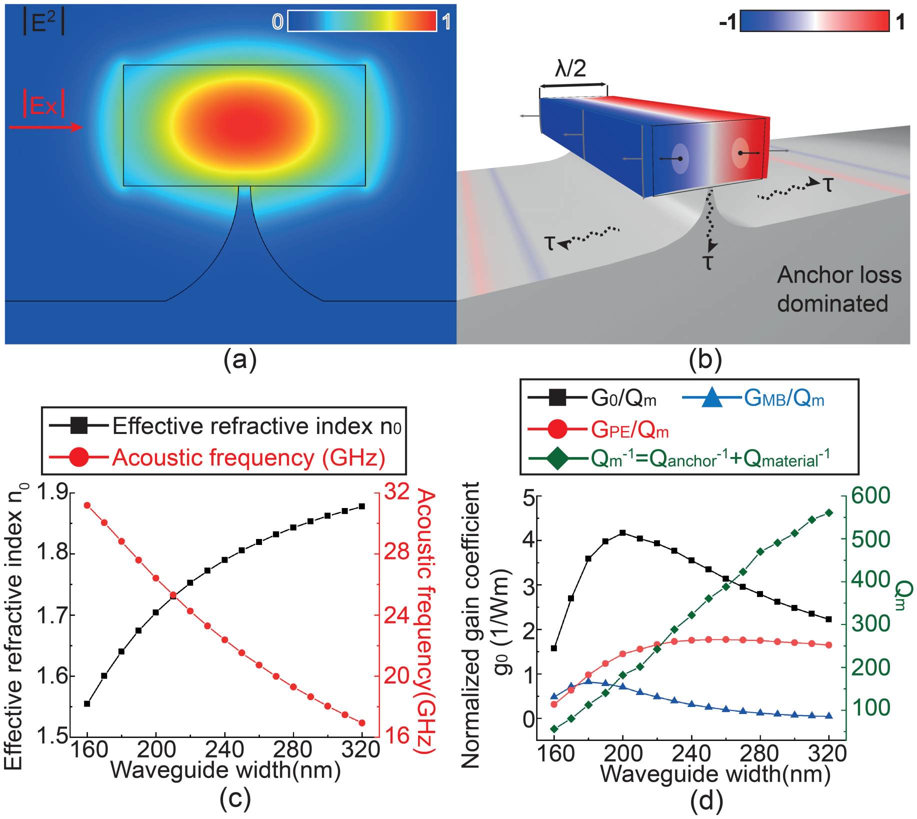

Fig. 3. The results of intramodal TE FSBS: (a) The normalized electric field of the TE mode, with E_x directed parallel to the waveguide surface. (b) The horizontal component of the selected acoustic mode **u** (blue,-; red,+) aligned with photoelastic (black arrows) and moving boundary (grey arrows). (c) The refractive index n_0 and acoustic mode frequency ν_{TE}^{FSBS} as a function of waveguide width w. As w increases, n_0 increases, indicating a better confinement of the the optical mode within AlN waveguide. While ν_{TE}^{FSBS} decreases reciprocally as predicted by Fabry-Pérot cavity condition. (d) The normalized Brillouin gain coefficient g_0 (black), moving boundary contribution G_{MB} (blue), photoelastic contribution G_{PE} (red) and Q_m (green) as a function of w. The biggest gain appears at 280nm width with G_0 of 1311 $W^{-1}m^{-1}$ and Q_m of 469.73. Q_m is below our pre-set value for $Q_{material}$, indicating that the anchor loss is the dominant loss in this case.

In summary, a narrower waveguide could lead to a stronger coupling between optical and acoustic modes, but this will also enhance the leakage of the acoustic wave and decrease the Q_m. Therefore, there would be a trade-off between stronger opto-acoustical interaction and Q_m. The biggest gain coefficient we obtain is 1311 $W^{-1}m^{-1}$ with Q_m of 469.73 at 280nm width. Q_m is below our pre-set value for $Q_{material}$, which means that the anchor loss is the dominant loss in this case.

Then we investigate in the BSBS of TE mode, and the results are summarized in Fig. 4. The main difference between FSBS and BSBS is that for FSBS, the propagation constant for acoustic mode is almost zero, while that for BSBS the propagation constant is almost 2 times the k_p [33]. This means that the selected acoustic mode for FSBS only has transverse vibration as shown in Fig. 3(b), while the acoustic mode for BSBS will have longitudinal vibration [52].

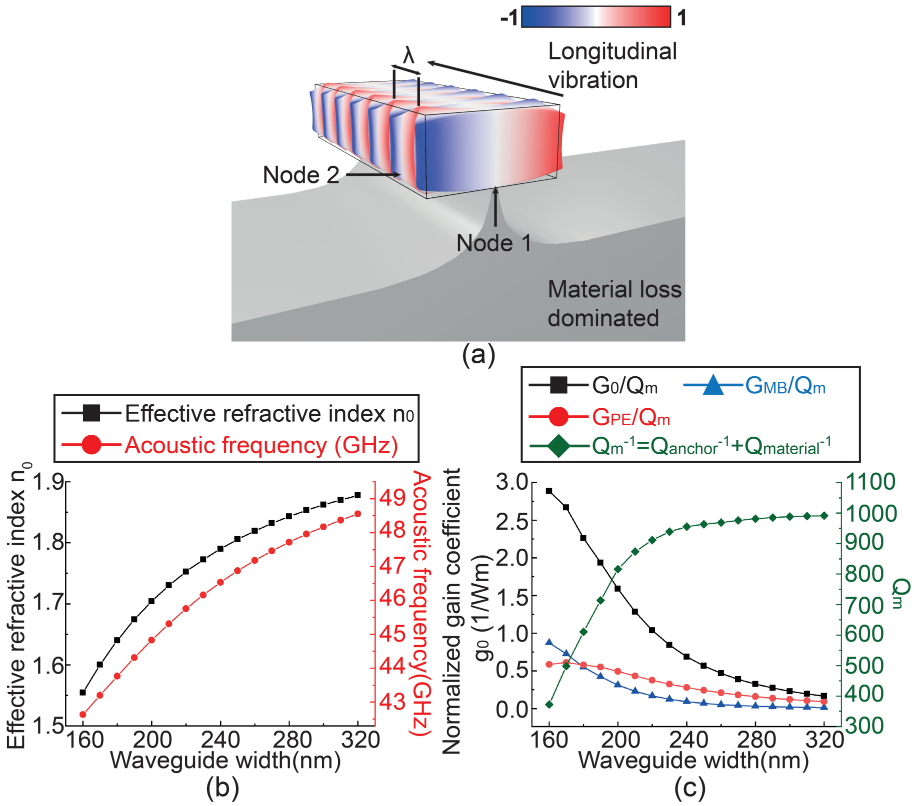

Fig. 4. The results of intramodal TE BSBS: (a) The horizontal component of the acoustic mode **u**. This mode has longitudinal vibration along the propagation direction and also has two nodes point on both front face and side face. (b) The refractive index n_0 and acoustic frequency ν_{TE}^{BSBS} as a function of waveguide width w. ν_{TE}^{BSBS} could be estimated by $2n_0V_l/\lambda$ [53]. It can be seen that ν_{TE}^{BSBS} does not decrease inversely to w, but increases linearly with n_0. (c) The normalized Brillouin gain coefficient g_0 (black), moving boundary contribution G_{MB} (blue), photoelastic contribution G_{PE} (red) and Q_m (green) as a function of w. Both G_{MB} and G_{PE} tend to decline with the increase of w. g_0 is generally smaller compared to that in TE FSBS. While Q_m increases and converges into a value of 1000, which is limited by $Q_{material}$. This means that for TE BSBS, the dominant loss is material loss instead of anchor loss in TE FSBS. For the same structure, the BSBS process will have much longer acoustic decay length than that of the FSBS process [54].

Fig. 4(a) shows the nature of longitudinal vibration of the acoustic mode for BSBS. It can be seen that at the transverse direction, this mode has similar distribution with FSBS selected mode, which satisfies the mode distribution matching requirements [34]. And on the side surface, the longitudinal wave propagating through the waveguide can be observed clearly. Its frequency ν_{TE}^{BSBS} can be estimated by $2n_0V_l/\lambda$ [53], where n_0 is the effective refractive index, V_l=$\sqrt{C_{44}/\rho}$ is the longitudinal acoustic velocity and λ is the wavelength of the optical wave. It can be seen that ν_{TE}^{BSBS} is no longer related with waveguide width anymore, but has direct relation with n_0. The change of n_0 and ν_{TE}^{BSBS} versus w is summarized in Fig. 4(b). Same with FSBS, the increased width will result in higher n_0, but ν_{TE}^{BSBS} increases with w, and it has linear relation with n_0 as we expect.

Fig. 4(c) shows normalized gain coefficient g_0 (black), moving boundary contribution G_{MB} (blue), photoelastic contribution G_{PE} (red) as well as the Q_m (green) again. First we notice that both G_{MB} and G_{PE} decline with the increase of w. Also g_0 is generally smaller compared to that in TE FSBS.

However, as w keeps increasing, Q_m increases rapidly and it converges to a value of 1000, which is limited by $Q_{material}$. This means that for TE BSBS, the dominant loss is material loss instead of anchor loss. This indicates that for the same structure, the BSBS process will have much longer acoustic decay length than that of the FSBS process [54]. Also it is worth mentioning that it does not conflict with the results of FSBS that the Q_m increases with higher frequency. The explanation for this is the node theory [55]. From Fig. 4(a), it can be seen that there are two node points for the acoustic mode of BSBS: $Node$ 1 at the front face where the anchor is placed, and $Node$ 2 at the side face. When ν_{TE}^{BSBS} gets bigger, the area of $Node$ 2 will be squeezed and gets narrower. But the area of $Node$ 1 where the anchor is placed gets wider, leading to less energy leakage and higher Q_m. Details of the analysis are not shown here for the sake of simplicity but it could be found in supplementary 1 section 3.

5. Forward and backward stimulated Brillouin scattering for TM mode

Having analysed the FSBS and BSBS for TE mode, the author will analyse the FSBS and BSBS for TM mode in this section. Previously it is believed that TM mode would be unsuitable for such a design due to the fact that the selected acoustic mode will have vertical vibration and it would directly leak out via the anchor [48]. However, our findings show that for TM FSBS, there will be a case where the anchor loss could be greatly suppressed and results in a big Brillouin gain coefficient.

Fig. 5 summarizes the results for TM FSBS. The normalized electric field of TM mode is shown in Fig. 5(a), and E_x is oriented perpendicular to the waveguide surface. Due to this difference, the selected acoustic mode will have a vertical distribution, as shown in Fig. 5(b). Fig. 5(c) shows n_0 and ν_{TM}^{FSBS} as the function of w. Same with previous cases, with w increases, n_0 increases. While ν_{TM}^{FSBS}, predicted by Fabry-Pérot cavity condition ($\nu_{TM}^{FSBS} \approx V_t/2h$) [17], slightly decreases from 37.5 GHz to 35 GHz. Fig. 5(d) summarizes the change of g_0 (black), G_{MB} (blue), G_{PE} (red) and the Q_m (green) for TM FSBS. Similar to the previous cases, both G_{MB} and G_{PE} will decline with the increase of the waveguide width. It also brings to our attention that the Q_m of TM FSBS is generally smaller compared to the results of TE FSBS, indicating a stronger energy leakage via anchor as expected [48].

However, there is a peak of Q_m when the w is 330nm. The value at this point is almost 1000, indicating that the material loss is dominant and anchor loss has been suppressed greatly. This is because with width increasing, the acoustic mode is shifting from lower order mode to a higher one, as it is shown in Fig. 6. During the transition, there will be one mode where the node point coincides with the pillar anchor position, leading to the reduction of the anchor loss. From left to right in Fig. 6, each sub-figure is the vertical displacement of the selected acoustic modes at width of (a)280 nm, (b)330 nm, (c)360 nm. It can be seen that there is little energy leaking into the substrate at 330 nm while clear energy leakage can be observed in other cases. This finding proves that the partially suspended system could also be suitable for sufficient SBS gain for TM mode and provides a new way to enhance the Brillouin gain.

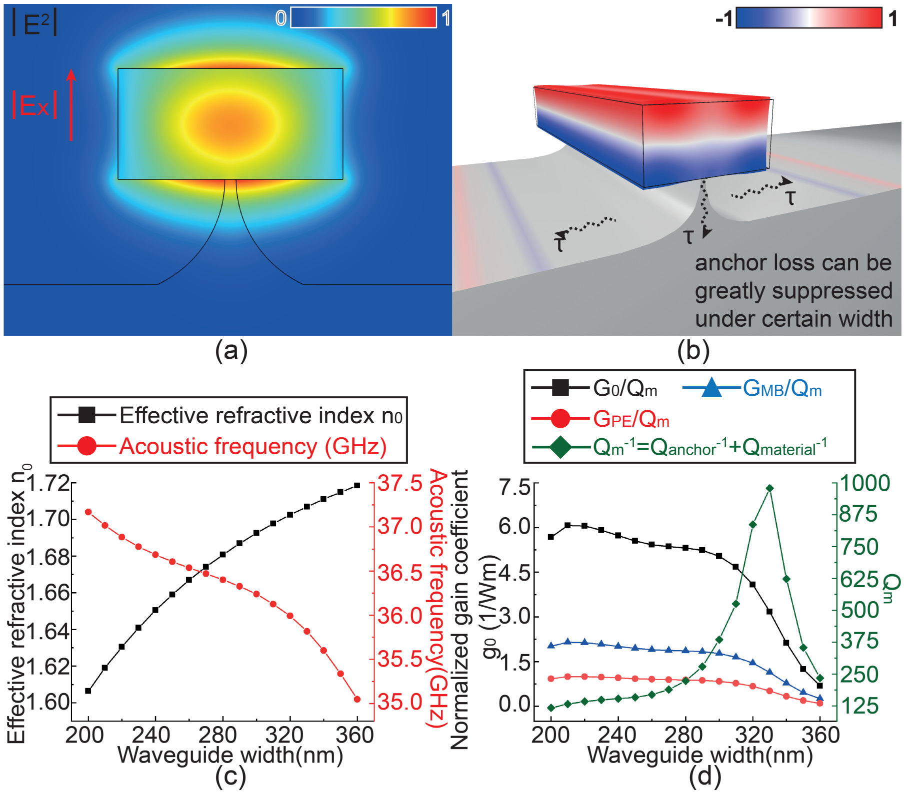

Fig. 5. The results of intramodal TM FSBS: (a) The normalized electric field of the TM mode, with E_x directed perpendicular to the waveguide surface. (b) The vertical component of the acoustic mode **u**. The node point of this mode is on the side surface, and it is expected that the energy will leak via anchor greatly [48] (c) The refractive index n_0 and acoustic mode frequency v_{TM}^{FSBS} as a function of waveguide width w. v_{TM}^{FSBS} slightly decreases from 37.5 GHz to 35 GHz with w increasing. (d) The normalized Brillouin gain coefficient g_0 (black), moving boundary contribution G_{MB} (blue), photoelastic contribution G_{PE} (red) and Q_m (green) as a function of w. There is a peak at 330 nm due to the change in mode distributions as shown in Fig. 6.

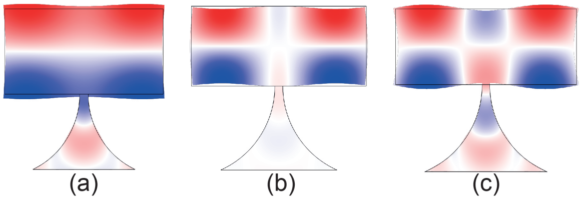

Fig. 6. The mode distributions of selected acoustic modes for TM FSBS at different w: (a)280 nm; (b)330 nm; (c)360 nm. With w increasing, the acoustic mode is transferring from lower mode to a higher one. During the transition, there will be a mode of which the node point coincides with the anchor and suppresses the energy leakage greatly.

We also investigate the BSBS process for TM mode and all the results are summarized in Fig. 7. Same with TE BSBS process, the selected mode for TM BSBS has a longitudinal vibration as shown in Fig. 7(a). n_0 and v_{TM}^{BSBS} as the function of w is summarized in Fig. 7(b). And v_{TM}^{BSBS} can also be estimated by $2n_0V_l/\lambda$ [53]. But TM mode generally has smaller n_0 compared to that of TE mode, therefore the Brillouin shifted frequency is also smaller compared to that of TE BSBS.

Fig. 7(c) shows g_0 (black), G_{MB} (blue), G_{PE} (red) as well as the Q_m (green). Same with the findings for TE mode, it can be seen that for TM mode, FSBS process has stronger coupling between optical mode and acoustic mode than BSBS process. As for Q_m, although it increases with bigger w, it is still below 400, showing that the anchor loss is the main loss in this case. And from the Fig. 7(a), it can be seen that for TM BSBS, the position of the pillar does not match with the node point, which is on the middle of the side surface. A low-loss performance could be expected if the anchor is placed on the middle of the side wall.

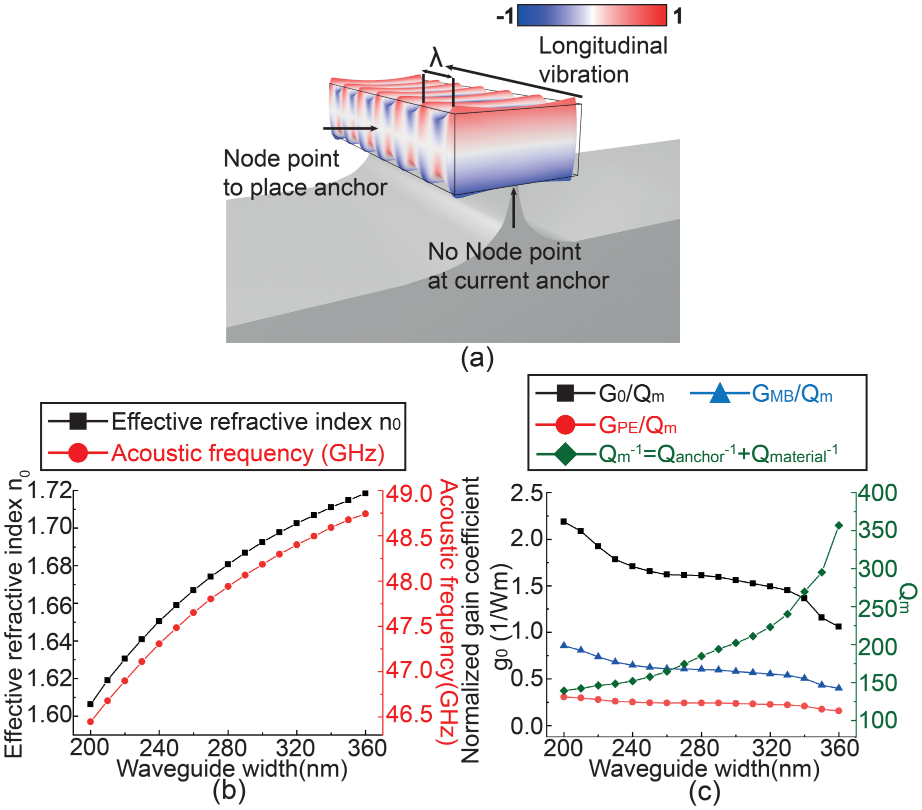

Fig. 7. The results of intramodal TM BSBS: (a) The vertical component of the selected acoustic mode **u**. It also has longitudinal vibration along the propagation direction. There is no node point at the place where the anchor is. A higher acoustic dissipation can be expected. (b) n_0 and v_{TM}^{BSBS} as a function of w. Same with TE BSBS, v_{TM}^{BSBS} increases linearly with n_0 [53]. (c) The normalized Brillouin gain coefficient g_0 (black), moving boundary contribution G_{MB} (blue), photoelastic contribution G_{PE} (red) and Q_m (green) as a function of w. Q_m is the smallest among all the four processes, showing that TM BSBS is the one that suffers most from the anchor loss.

6. Influence of waveguide height

In this section, we explore the influence of the waveguide height. TE FSBS is taken as an example here, other processes are also studied and similar results can be observed.

Fig. 8 shows the results for different *h*: With the decrease of waveguide height, the normalized gain coefficient g_0 gets larger, indicating a stronger interaction between optical and acoustic modes. This is due to the fact that the intensity of the optical mode will be increased inside a smaller area and lead to a larger gain. But this will also lead to a higher propagation loss of the optical mode. For example, smaller waveguide size will result in a stronger interaction between the evanescent field near the AlN/air boundary and roughness on the side wall. Therefore there is a trade-off between the increase of the interaction and propagation loss to find the optimized height and width for this design.

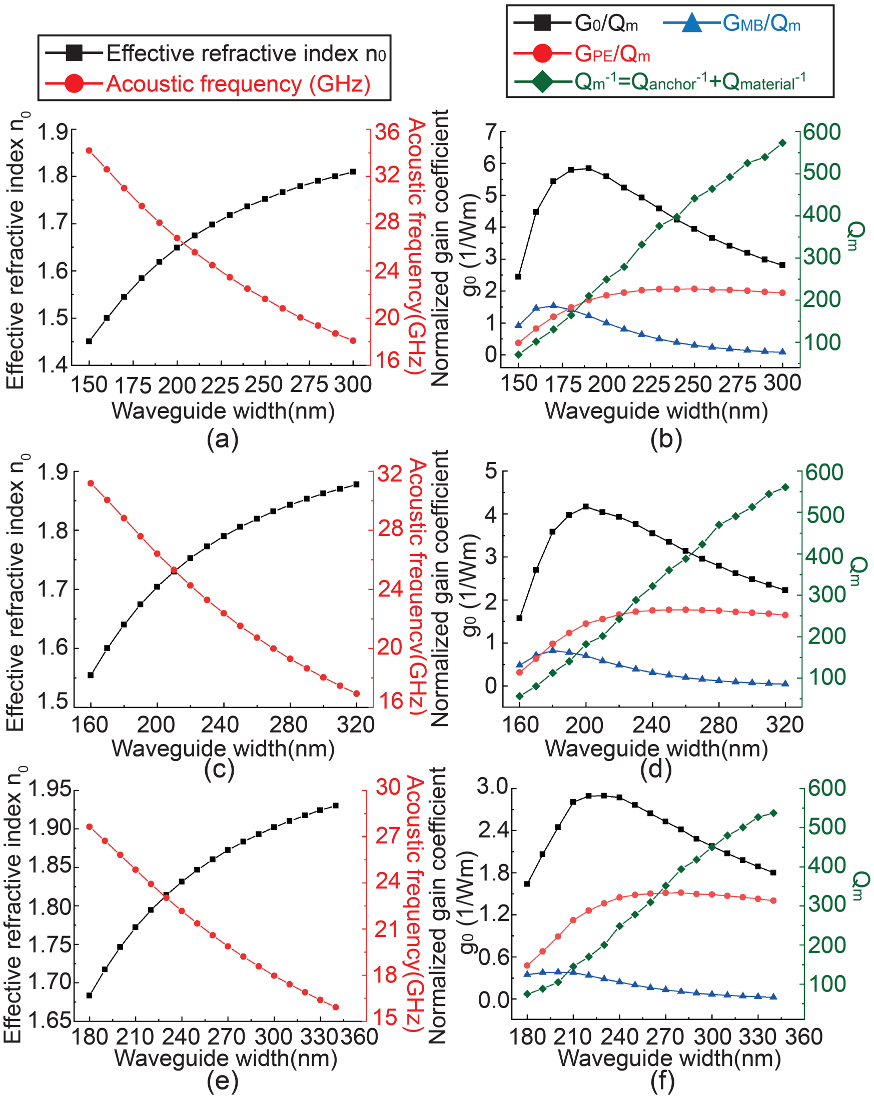

Fig. 8. The influences of the waveguide height *h* on the Brillouin gain of TE FSBS: From top left to the bottom right are: (a)-(b) results of *h* 130nm; (c)-(d) results of *h* 150nm; (e)-(f) results of *h* 170nm.

7. Fabrication feasibility and tolerance analysis

Although the focus is on the theoretical analysis of partially suspended AlN supported by silica anchor, here we introduce a potential route for realizing the opto-mechanical system that we propose.

In this paper, we model the AlN layer assuming it is polycrystalline with c-axis aligned with the z-axis of the waveguide system and random in-plane axis orientation. A straightforward route for the development of polycrystalline AlN on silica substrate is via sputtering. Pure aluminium (99.999%) targets are sputtered in an argon and nitrogen gas mixture [56]. By carefully controlling the flow rates of argon and nitrogen gas, the best stoichiometry and crystal orientation could be obtained [57]. Besides, the stress in the AlN film can be tailored to be around ±75 MPa by adjusting the RF bias power, which will permit the fabrication of high confinement waveguides in both TE and TM mode [31]. Once the stack with low stress is available, the patterning of the waveguides is straightforward by optical or e-beam lithography [58] and dry etching [59]. A total propagation loss down to 0.6 dB/cm could be obtained [31].

To form the silica pillar structure, an additional oxide etch with hydrofluoric (HF) acid is required. By controlling the concentration of HF acid, a narrow pillar could be left underneath the waveguide [17]. This step will lead to the fabrication tolerance of the pillar width. We assume that the fixed size of h=150 nm, w=280 nm, and the tolerance of the pillar width g is within ±8 nm [60]. The results are summarized in Table 3. It can be seen that the fabrication tolerance on the pillar width will lead to the total gain coefficient varying from 1965 to 931. Although the variation of pillar width will affect the values of G_{MB} and G_{PE}, the main influence is on the Q_m. The narrower the pillar width it is, the higher the Q_m is, and it will lead to a higher gain coefficient.

Table 3. The effect of pillar width g's variation on TE FSBS gain coefficient

Pillar width (nm)	G_{MB} $(W^{-1}m^{-1})$	G_{PE} $(W^{-1}m^{-1})$	Q_m	Total gain $(W^{-1}m^{-1})$
7	0.119	1.802	690.15	1965.09
11	0.120	1.778	564.36	1591.86
19	0.121	1.724	397.68	1096.91
23	0.122	1.695	341.88	931.26

There is also a fabrication tolerance to the waveguide width. From previous sections, we already know that the both Q factor and shifted Brillouin frequency are related with waveguide width and height. But different coupling mechanisms will suffer from the fabrication tolerance differently.

TM FSBS would suffer the most from the deviation in the waveguide width. From Fig. 5, if the targeted waveguide width is at 330 nm, where the peak of Q factor is. A variation of 3% in the waveguide width could lead to the total gain coefficient dropping from 3400 $W^{-1}m^{-1}$ to 3100 $W^{-1}m^{-1}$ with 9% variation. While for TE FSBS, a variation of 3% in the waveguide width will only introduce 2% variation in the final gain coefficient. For TE and TM BSBS, the effect of the fabrication tolerance is mainly decided by the influence of the width on the Q factor.

8. Conclusion

In this paper, we propose a novel III-V material AlN to achieve a strong Brillouin scattering interaction in the visible wavelength range. AlN has several advantages for the applications of stimulated Brillouin scattering, including wide transparent window, free of nonlinear loss, big photoelastic coefficient, mature fabrication technology as well as the compatibility with CMOS. A sufficient Brillouin gain can only be obtained by the simultaneous confinement of optical mode and acoustic mode. Therefore, a partially suspended AlN waveguide supported with a silica pillar anchor is used to reduced the phonon leakage.

We apply a full-vectorial formalism to calculate the Brillouin gain including the photoelastic effect as well as the moving boundary contribution. The accuracy of the method is validated by matching the simulated results with reported results from [17]. Our model reveals the importance of matching rotation matrix with crystal coordinate system. Based on the validated model, our results show a total gain value of 1311 $W^{-1}m^{-1}$ for the TE FSBS process when both anchor loss and material loss are considered in the proposed system. Our study also finds out that the anchor loss is strongly related with the relevant position between pillar anchor and the node point of the selected acoustic mode. Especially for the TM FSBS process, anchor loss could be greatly suppressed under certain waveguide size when the selected acoustic mode's node point matches with the pillar anchor's position. We envisage that this system would be very useful for the application in growing on-chip laser [61] and ultra-fast communication [62] in the visible wavelength range.

Funding.
This work is supported by the Engineering and Physical Sciences Research Council (EPSRC EP/V000624/1)

Acknowledgments.
The authors acknowledge the use of the IRIDIS High Performance Computing Facility, and associated support services at the University of Southampton, in the completion of this work.

Disclosures.
The authors declare no conflicts of interest

Data Availability Statement.
The data that support the findings of this study are openly available ay the University of Southampton ePrints research repository [63].

Supplemental document.
See Supplement 1 for supporting content.

References

1. R. W. Boyd, *Nonlinear optics* (Academic, 2020).
2. R. Chiao, C. Townes, and B. Stoicheff, "Stimulated Brillouin scattering and coherent generation of intense hypersonic waves," Phys. Rev. Lett. **12**, 592–595 (1964).
3. I. V. Kabakova, R. Pant, D.-Y. Choi, S. Debbarma, B. Luther-Davies, S. J. Madden, and B. J. Eggleton, "Narrow linewidth Brillouin laser based on chalcogenide photonic chip," Opt. letters **38**, 3208–3211 (2013).
4. N. T. Otterstrom, R. O. Behunin, E. A. Kittlaus, Z. Wang, and P. T. Rakich, "A silicon Brillouin laser," Science **360**, 1113–1116 (2018).
5. S. Gundavarapu, G. M. Brodnik, M. Puckett, T. Huffman, D. Bose, R. Behunin, J. Wu, T. Qiu, C. Pinho, N. Chauhan, J. Nohava, P. T. Rakich, K. D. Nelson, M. Salit, and D. J. Blumenthal, "Sub-hertz fundamental linewidth photonic integrated Brillouin laser," Nat. Photonics **13**, 60–67 (2019).
6. A. Byrnes, R. Pant, E. Li, D.-Y. Choi, C. G. Poulton, S. Fan, S. Madden, B. Luther-Davies, and B. J. Eggleton, "Photonic chip based tunable and reconfigurable narrowband microwave photonic filter using stimulated Brillouin scattering," Opt. express **20**, 18836–18845 (2012).
7. A. Choudhary, I. Aryanfar, S. Shahnia, B. Morrison, K. Vu, S. Madden, B. Luther-Davies, D. Marpaung, and B. J. Eggleton, "Tailoring of the Brillouin gain for on-chip widely tunable and reconfigurable broadband microwave photonic filters," Opt. letters **41**, 436–439 (2016).
8. D. Marpaung, B. Morrison, M. Pagani, R. Pant, D.-Y. Choi, B. Luther-Davies, S. J. Madden, and B. J. Eggleton, "Low-power, chip-based stimulated Brillouin scattering microwave photonic filter with ultrahigh selectivity," Optica **2**, 76–83 (2015).

9. C. G. Poulton, R. Pant, A. Byrnes, S. Fan, M. Steel, and B. J. Eggleton, “Design for broadband on-chip isolator using stimulated Brillouin scattering in dispersion-engineered chalcogenide waveguides,” Opt. express **20**, 21235–21246 (2012).
10. E. A. Kittlaus, N. T. Otterstrom, P. Kharel, S. Gertler, and P. T. Rakich, “Non-reciprocal interband Brillouin modulation,” Nat. Photonics **12**, 613–619 (2018).
11. M. Merklein, B. Stiller, K. Vu, S. J. Madden, and B. J. Eggleton, “A chip-integrated coherent photonic-phononic memory,” nature Commun. **8**, 1–7 (2017).
12. M. Merklein, B. Stiller, and B. J. Eggleton, “Brillouin-based light storage and delay techniques,” J. Opt. **20**, 083003 (2018).
13. J. Li, M.-G. Suh, and K. Vahala, “Microresonator Brillouin gyroscope,” Optica **4**, 346–348 (2017).
14. P. T. Rakich, C. Reinke, R. Camacho, P. Davids, and Z. Wang, “Giant enhancement of stimulated Brillouin scattering in the subwavelength limit,” Phys. Rev. X **2**, 011008 (2012).
15. R. Pant, C. G. Poulton, D.-Y. Choi, H. Mcfarlane, S. Hile, E. Li, L. Thevenaz, B. Luther-Davies, S. J. Madden, and B. J. Eggleton, “On-chip stimulated Brillouin scattering,” Opt. express **19**, 8285–8290 (2011).
16. B. Morrison, A. Casas-Bedoya, G. Ren, K. Vu, Y. Liu, A. Zarifi, T. G. Nguyen, D.-Y. Choi, D. Marpaung, A. M. Madden, Stephen J, and B. J. Eggleton, “Compact Brillouin devices through hybrid integration on silicon,” Optica **4**, 847–854 (2017).
17. R. Van Laer, B. Kuyken, D. Van Thourhout, and R. Baets, “Interaction between light and highly confined hypersound in a silicon photonic nanowire,” Nat. Photonics **9**, 199–203 (2015).
18. R. Van Laer, A. Bazin, B. Kuyken, R. Baets, and D. Van Thourhout, “Net on-chip Brillouin gain based on suspended silicon nanowires,” New J. Phys. **17**, 115005 (2015).
19. E. A. Kittlaus, N. T. Otterstrom, and P. T. Rakich, “On-chip inter-modal Brillouin scattering,” Nat. communications **8**, 1–9 (2017).
20. F. Gyger, J. Liu, F. Yang, J. He, A. S. Raja, R. N. Wang, S. A. Bhave, T. J. Kippenberg, and L. Thévenaz, “Observation of stimulated Brillouin scattering in silicon nitride integrated waveguides,” Phys. review letters **124**, 013902 (2020).
21. K. Wang, J. Sun, and M. Cheng, “Design of partially suspended silicon nitride slot waveguides for efficient forward stimulated Brillouin scattering,” IEEE Photonics J. **12**, 1–11 (2020).
22. W. Jin, L. Chang, W. Xie, H. Shu, J. D. Peters, X. Wang, and J. E. Bowers, “Stimulated Brillouin scattering in AlGaAs on insulator waveguides,” in *CLEO: Science and Innovations,* (Optical Society of America, 2020), pp. SM4–L7.
23. J. Song, X. Guo, W. Peng, J. Pan, L. Wan, T. Feng, S. Zeng, D. Liu, B. Zhang, M. Zhang, and Z. Li, “Stimulated Brillouin scattering in low-loss Ge25Sb10S65 chalcogenide waveguides,” J. Light. Technol. **39**, 5048–5053 (2021).
24. C. Wolff, R. Soref, C. Poulton, and B. Eggleton, “Germanium as a material for stimulated Brillouin scattering in the mid-infrared,” Opt. express **22**, 30735–30747 (2014).
25. C. Wolff, P. Gutsche, M. J. Steel, B. J. Eggleton, and C. G. Poulton, “Impact of nonlinear loss on stimulated Brillouin scattering,” JOSA B **32**, 1968–1978 (2015).
26. F. De Leonardis, R. A. Soref, M. Soltani, and V. M. Passaro, “Stimulated Brillouin scattering in an AlGaN photonics platform operating in the visible spectral range,” Sci. reports **8**, 1–13 (2018).
27. K. Jones, T. Chow, M. Wraback, M. Shatalov, Z. Sitar, F. Shahedipour, K. Udwary, and G. Tompa, “AlGaN devices and growth of device structures,” J. Mater. Sci. **50**, 3267–3307 (2015).
28. S. Y. Davydov, “Evaluation of physical parameters for the group III nitrates: BN, AlN, GaN, and InN,” Semiconductors **36**, 41–44 (2002).
29. R. Puurunen, A. Root, P. Sarv, S. Haukka, E. Iiskola, M. Lindblad, and A. Krause, “Growth of aluminium nitride on porous silica by atomic layer chemical vapour deposition,” Appl. Surf. Sci. **165**, 193–202 (2000).
30. X. Guo, C.-L. Zou, and H. X. Tang, “Second-harmonic generation in aluminum nitride microrings with 2500%/w conversion efficiency,” Optica **3**, 1126–1131 (2016).
31. C. Xiong, W. H. Pernice, and H. X. Tang, “Low-loss, silicon integrated, aluminum nitride photonic circuits and their use for electro-optic signal processing,” Nano letters **12**, 3562–3568 (2012).
32. C. Wolff, M. J. Steel, B. J. Eggleton, and C. G. Poulton, “Stimulated Brillouin scattering in integrated photonic waveguides: Forces, scattering mechanisms, and coupled-mode analysis,” Phys. Rev. A **92**, 013836 (2015).
33. W. Qiu, P. T. Rakich, H. Shin, H. Dong, M. Soljačić, and Z. Wang, “Stimulated Brillouin scattering in nanoscale silicon step-index waveguides: a general framework of selection rules and calculating SBS gain,” Opt. express **21**, 31402–31419 (2013).
34. C. Wolff, M. Steel, and C. Poulton, “Formal selection rules for Brillouin scattering in integrated waveguides and structured fibers,” Opt. express **22**, 32489–32501 (2014).
35. R. N. Candler, H. Li, M. Lutz, W.-T. Park, A. Partridge, G. Yama, and T. W. Kenny, “Investigation of energy loss mechanisms in micromechanical resonators,” in *TRANSDUCERS’03. 12th International Conference on Solid-State Sensors, Actuators and Microsystems. Digest of Technical Papers,* vol. 1 (IEEE, 2003), pp. 332–335.
36. J.-Y. Lee and A. Seshia, “5.4-MHz single-crystal silicon wine glass mode disk resonator with quality factor of 2 million,” Sensors Actuators A: Phys. **156**, 28–35 (2009).
37. C.-M. Lin, Y.-Y. Chen, V. V. Felmetsger, D. G. Senesky, and A. P. Pisano, “AlN/3C–SiC composite plate enabling high-frequency and high-Q micromechanical resonators,” Adv. Mater. **24**, 2722–2727 (2012).
38. S. Gong, N.-K. Kuo, and G. Piazza, “GHz AlN lateral overmoded bulk acoustic wave resonators with a f· Q of 1.17×10^{13},” in *2011 Joint Conference of the IEEE International Frequency Control and the European Frequency and Time*

Forum (FCS) Proceedings, (IEEE, 2011), pp. 1–5.

39. A. Reinhardt, M. Delaye, J. Abergel, V. Kovacova, M. Allain, L. Andreutti, D. Mercier, J. Georges, F. Tomaso, P. Lassagne, E. Defaÿ, N. Chretien, T. Baron, G. Martin, E. Lebrasseur, S. Ballandras, L. Chommeloux, and J. Lesage, "Ultra-high Q·f product laterally-coupled AlN/silicon and AlN/sapphire high overtone bulk acoustic wave resonators," in *2013 IEEE International Ultrasonics Symposium (IUS),* (IEEE, 2013), pp. 1922–1925.
40. A. Frangi, A. Bugada, M. Martello, and P. Savadkoohi, "Validation of PML-based models for the evaluation of anchor dissipation in MEMS resonators," Eur. J. Mech. **37**, 256–265 (2013).
41. L. Mercadé, A. V. Korovin, Y. Pennec, J. Ahopelto, B. Djafari-Rouhani, and A. Martínez, "Vertical engineering for large Brillouin gain in unreleased silicon-based waveguides," Phys. Rev. Appl. **15**, 034021 (2021).
42. Y. Taniyasu and M. Kasu, "Improved emission efficiency of 210-nm deep-ultraviolet aluminum nitride light-emitting diode," NTT Tech. Rev **8**, 1–5 (2010).
43. B. A. Auld, "Chapter 3 - Elastic properties of solids," in *Acoustic fields and waves in solids,* vol. 1 (Wiley, 1992), pp. 75–78.
44. J. Pastrňák and L. Roskovcová, "Refraction index measurements on AlN single crystals," physica status solidi (b) **14**, 5–8 (1966).
45. I. H. Malitson, "Interspecimen comparison of the refractive index of fused silica," Josa **55**, 1205–1209 (1965).
46. A. Wright, "Elastic properties of zinc-blende and wurtzite AlN, GaN, and InN," J. Appl. physics **82**, 2833–2839 (1997).
47. M. Smith, B. Kuhlmey, C. M. de Sterke, C. Wolff, M. Lapine, and C. Poulton, "Metamaterial control of stimulated Brillouin scattering," Opt. letters **41**, 2338–2341 (2016).
48. W. Wang, Y. Yu, Y. Li, Z. Bai, G. Wang, K. Li, C. Song, Z. Wang, S. Li, Y. Wang, Z. Lu, Y. Li, T. Liu, and X. Yan, "Tailorable Brillouin light scattering in a lithium niobate waveguide," Appl. Sci. **11**, 8390 (2021).
49. S. Crampin, "Chapter 3 - Elasticity," in *Foundations of Anisotropy for Exploration Seismics,* vol. 22 of *Handbook of Geophysical Exploration: Seismic Exploration* K. Helbig, ed. (Pergamon, 1994), pp. 87–89.
50. B. C. Sturmberg, K. B. Dossou, M. J. Smith, B. Morrison, C. G. Poulton, and M. J. Steel, "Finite element analysis of stimulated Brillouin scattering in integrated photonic waveguides," J. Light. Technol. **37**, 3791–3804 (2019).
51. G. S. Wiederhecker, P. Dainese, and T. P. Mayer Alegre, "Brillouin optomechanics in nanophotonic structures," APL Photonics **4**, 071101 (2019).
52. R. Parihar, R. Dhawan, S. Goel, B. O. Subham, and A. Choudhary, "Design of microwave photonic subsystems using Brillouin scattering," J. Light. Technol. **39**, 977–991 (2020).
53. A. Kobyakov, M. Sauer, and D. Chowdhury, "Stimulated Brillouin scattering in optical fibers," Adv. optics photonics **2**, 1–59 (2010).
54. C. Wolff, M. Steel, B. Eggleton, and C. Poulton, "Acoustic build-up in on-chip stimulated Brillouin scattering," Sci. reports **5**, 1–7 (2015).
55. S. Humad, R. Abdolvand, G. K. Ho, G. Piazza, and F. Ayazi, "High frequency micromechanical piezo-on-silicon block resonators," in *IEEE International Electron Devices Meeting 2003,* (IEEE, 2003), pp. 39.3.1–39.3.4.
56. E. Milyutin, S. Harada, D. Martin, J. Carlin, N. Grandjean, V. Savu, O. Vaszquez-Mena, J. Brugger, and P. Muralt, "Sputtering of (001) AlN thin films: Control of polarity by a seed layer," J. Vac. Sci. & Technol. B, Nanotechnol. Microelectron. Materials, Process. Meas. Phenom. **28**, 61–63 (2010).
57. I. Gablech, V. Svatoš, O. Caha, M. Hrabovskỳ, J. Prášek, J. Hubálek, and T. Šikola, "Preparation of (001) preferentially oriented titanium thin films by ion-beam sputtering deposition on thermal silicon dioxide," J. materials science **51**, 3329–3336 (2016).
58. L. Zhang, F. Xu, J. Wang, C. He, W. Guo, M. Wang, B. Sheng, L. Lu, Z. Qin, X. Wang, and B. Shen, "High-quality AlN epitaxy on nano-patterned sapphire substrates prepared by nano-imprint lithography," Sci. reports **6**, 1–8 (2016).
59. R. M. Pinto, V. Gund, C. Calaza, K. Nagaraja, and K. Vinayakumar, "Piezoelectric aluminum nitride thin-films: A review of wet and dry etching techniques," Microelectron. Eng. p. 111753 (2022).
60. L. Zhou, Y. Lu, Y. Fu, H. Ma, and C. Du, "Design of a hybrid on-chip waveguide with giant backward stimulated Brillouin scattering," Opt. Express **27**, 24953–24971 (2019).
61. I. Aharonovich, A. Woolf, K. J. Russell, T. Zhu, N. Niu, M. J. Kappers, R. A. Oliver, and E. L. Hu, "Low threshold, room-temperature microdisk lasers in the blue spectral range," Appl. Phys. Lett. **103**, 021112 (2013).
62. Y.-C. Chi, D.-H. Hsieh, C.-T. Tsai, H.-Y. Chen, H.-C. Kuo, and G.-R. Lin, "450-nm GaN laser diode enables high-speed visible light communication with 9-Gbps QAM-OFDM," Opt. express **23**, 13051–13059 (2015).
63. P. Li, "ResearchData SBSinAlN," `https://doi.org/10.5258/SOTON/D2225`.